Correlation between Electronic Properties and Hydrodesulfurization Activity of 4d-Transition-Metal Sulfides

Raúl Oviedo-Roa,[†] José-Manuel Martínez-Magadán,*,[†] and Francesc Illas[†,‡]

Programa de Ingeniería Molecular, Instituto Mexicano del Petróleo, México D.F. 07730, México, and Departament de Química Física i Centre Especial de Recerca en Química Teòrica, Universitat de Barcelona i Parc Científic de Barcelona, Martí i Franquès 1, 08028 Barcelona, Spain

Received: May 3, 2005; In Final Form: March 1, 2006

The present study attempts to examine the relationship between electronic-structure properties exhibited by 4d-transition-metal sulfides (TMSs) in connection with the hydrodesulfurization (HDS) catalytic activity. The electronic structure is studied by means of a periodic density functional approach using a plane-wave basis set and appropriate pseudopotentials. Both bulk and relevant surfaces of NbS, NbS_2, MoS_2, TcS_2, RuS_2, Rh_2S_3, PdS, and PdS_2 have been analyzed. High densities of nonbonding states below the Fermi level have been found for the TMSs that exhibit good catalytic performance. Therefore, it is suggested that the incomplete filling of the band gap at exposed transition metal atoms over the catalyst surface plays a determinant role in the HDS reactions. It has also been found that the highest HDS activity occurs when the surface-metal-site density of electronic states has a local minimum at the Fermi level that enhances the donation−back-donation mechanism. Additionally, the Sabatier principle is qualitatively rationalized in terms of the position of covalent bands below the Fermi level.

1. Introduction

Transition metal sulfide (TMS) catalysts are of industrial interest due to their stable catalytically active phases for strongly sulfo-reductive hydroprocessing conditions. In this process, usually termed hydrodesulfurization (HDS), sulfur contained in the different compounds usually present in crude oil is catalytically removed yielding sulfur-free hydrocarbon products and hydrogen sulfide. Among the different sulfides, Rh_2S_3 and pyrite-type disulfides such as RuS_2, OsS_2, and IrS_2 exhibit the highest HDS activity[1] and are also the most active in the hydrogenation and hydrodenitrogenation reactions.[2] Despite the enormous importance of the HDS process in the oil industry, detailed knowledge of the key factors governing the catalytic activity of the different TMSs is still lacking. In the 1980s, studies appeared in the catalysis literature suggesting that the HDS activities of second and third row transition metal sulfide catalysts exhibit a volcano-type dependence upon the position of the transition metal in the periodic table.[1,3,4] Explanations for the volcano-type dependence of HDS activity in terms of the metal−sulfur bond strength,[1] the metallic character of the sulfides,[3] and the structures of the sulfides[4] were proposed.

From theoretical studies of bulk TMSs it has been proposed that two electronic factors could be responsible for good HDS activity of a TMS. These are the ability of the transition metal to make covalent bonds with the 3p orbitals of sulfur via either σ or π bonds and the number of transition metal d electrons in the highest occupied molecular orbital[5] (HOMO), or equivalently, the density of states (DOS) at the Fermi level. It has been pointed out that, in the bulk phase, all catalytically active TMSs exhibit a semiconductor character and that the activity increases with the increasing t_{2g}-like character of the HOMO.[6,7] This trend could be attributed to the greater ability of the t_{2g}

states to back-donate electrons to the antibonding C−S $\pi*$ states of the sulfur-containing molecule.[5] However, despite these useful insights from bulk calculations, one must realize that the reaction takes place at the surface and that coordinatively unsaturated atoms are precisely the ones involved in the adsorption of reactants and products. Therefore, it is also important to elucidate the relevant electronic properties of the surface transition metal atoms in the processes accomplishing the catalysis. In this respect, ab initio molecular dynamics has confirmed both the donor properties of an organosulfur model, thiophene, through a charge flow into $Mo(d_{yz})$ orbitals of a catalytically active MoS_2 surface, and the back-donation into the thiophene antibonding C−S($\pi*$) states.[8]

It has been experimentally found that 3d TMSs are in general much less active than 4d and 5d TMSs, for which the maximum in catalytic activity is reached at the middle of the transition metal period.[3] Within the 3d metals the highest activity corresponds to Cr_2S_3, and the lowest activity is shown by MnS. Initial work[1] established an explanation for HDS activity in terms of the Sabatier principle: An intermediate metal−sulfur bond strength is necessary for HDS maximum activity, the metal−sulfur bond strength being extracted from the heat of formation. However, although a good correlation was obtained for 4d and 5d TMSs, no clear trend was observed for 3d TMSs, MnS being the worst case because, according to the Sabatier principle, MnS would be the most active sulfide for the first transition metal row series since its heat of formation is in the required range.[13] However, one must also consider the possible role of magneto-structural effects for the 3d TMS.[9,10]

In a previous theoretical work,[11] the electronic properties of the 3d TMS surfaces have been studied. It has been found that the magnetic properties of surfaces can affect HDS reactions. For MnS, it has been shown that the spin polarization splits the density of states into two broad peaks around the Fermi level. Thus, on a Mn-exposing surface, even if Mn could play a good role as a charge acceptor, it will be unable to complete the back-

* Author to whom correspondence should be addressed. E-mail: mmartine@imp.mx.
† Instituto Mexicano del Petróleo.
‡ Universitat de Barcelona i Parc Científic de Barcelona.

donation step. Nevertheless, progress was made in determining the metal−sulfur bond strength through density functional theory calculations of the cohesive energy, instead of relying on the heat of formation. Thus, TMSs with intermediate cohesive energy per metal−sulfur bond have the highest HDS activities, confirming that the cohesive energy is the most adequate parameter able to quantitatively render the electronic trend in TMSs.[6,12] Through the use of this redefinition of the metal−sulfur bond strength, MnS is not present anymore at the optimum range of strength.[13] Specially, a critical-point analysis of the charge density has been made.[14] This robust topological approach furnishes a simple correlation between the sulfur−metal bond energy and the Laplacian of the charge density and distinguishes clearly between ionic and covalent character of the bond.

In the present work, we extend the previous study carried out for the 3d TMS surfaces[11] to those of the 4d TMSs. In particular, this work aims to find the electronic properties of 4d TMS surfaces that are relevant to the conversion of organosulfur compounds and to determine the relative importance of the electronic structure of the surface and of the bulk of these materials. First, cluster model calculations on representative 4d TMSs were carried out to investigate the character of the corresponding molecular orbitals. Then, electronic calculations of bulk 4d TMSs were interpreted in terms of these orbitals. Finally, frontier orbitals for suitable supercell models of surfaces cut from the bulk structures are investigated.

These surfaces are aimed to contain coordinatively unsaturated sites (CUSs) because it is often argued that the chemically active sites of TMSs in the HDS process are precisely CUSs occupied by transition metal atoms. Nevertheless, it is important to point out that the electronic structure of the as-cleaved surfaces studied in this work corresponds to systems in ultrahigh-vacuum (UHV) conditions that could be different from those where the HDS process takes place. As-cleaved surfaces are not necessarily representative of the actual sulfur/transition metal ratio at the surface under the conditions prevailing in an HDS reactor since this ratio is indeed determined by the concentration of sulfur species (sulfhydryl groups, H_2S, or sulfur organic compounds) chemisorbed on the surfaces of the TMSs.[15,16] Therefore, the hypothesis behind the present work is that qualitative trends about the HDS capability of 4d TMS surfaces can be deduced from the electronic structure of the systems in UHV conditions. However, there is a great effort toward the simulation of the actual catalytic system. It has been shown that under HDS conditions the as-cleaved surface minimizes its energy by adsorbing sulfur, being predicted for MoS_2 that surfaces have a 50% S coverage on the Mo-terminated edge and that this coverage modifies the electronic surface states of CUSs reducing strongly the donor properties of exposed Mo atoms but their acceptor properties being less affected.[17,18] Similarly, sulfur-enriched termination with hydrogen coverage is found to be energetically favored compared to the stoichiometric and highly reduced RuS_2(111) surfaces.[19]

2. Material Models and Computational Methods

2.1. Crystal Structures of Selected 4d-Transition-Metal Sulfides. The 4d TMSs studied in the present work are NbS, NbS_2, MoS_2, TcS_2, RuS_2, Rh_2S_3, PdS, and PdS_2 (Figure 1). These compounds have either octahedral (NbS, TcS_2, RuS_2, Rh_2S_3), trigonal-prismatic (NbS_2, MoS_2), or four-coordination structure with a square-planar symmetry (PdS, PdS_2) environment around metallic sites (Figure 1).

Details of the structures of these TMSs can be found elsewhere.[6] The symmetry and experimental parameters of the bulk lattice for each of these sulfides are summarized in Table 1.
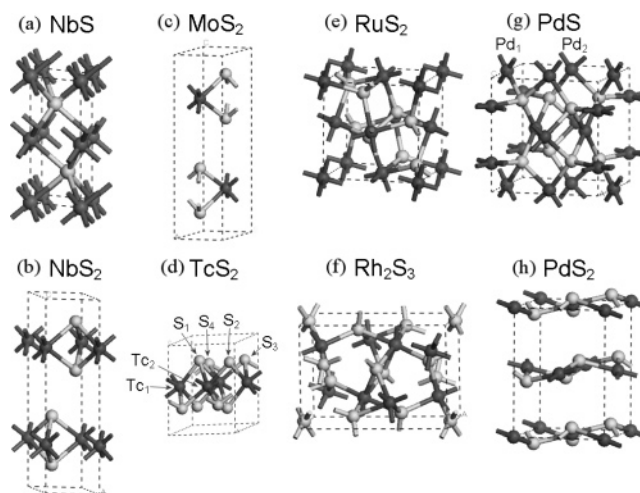

Figure 1. Unit cells for the geometric structures of bulk (a) NbS, (b) NbS_2, (c) MoS_2, (d) TcS_2, (e) RuS_2, (f) Rh_2S_3, (g) PdS, and (h) PdS_2. Dark and light spheres are transition metal and sulfur atoms, respectively. For TcS_2 and PdS the nonequivalent transition metal and chalcogen atoms are indicated.

TABLE 1: Crystallographic Data (in Å) for Transition Metal Sulfides of the 4d Series

compound	sulfur coordination of metal sites	space group	a	b	c
NbS	octahedral	$P6_3/mmc$	3.320	3.320	6.460
NbS_2	trigonal prismatic	$P6_3/mmc$	3.310	3.310	11.890
MoS_2	trigonal prismatic	$P6_3/mmc$	3.160	3.160	12.294
TcS_2	octahedral	$P\bar{1}$	6.371	6.464	6.654
RuS_2	octahedral	$Pa\bar{3}$	5.611	5.611	5.611
Rh_2S_3	octahedral	$Pbcn$	8.462	5.985	6.138
PdS	square planar	$P4_2/m$	6.429	6.429	6.611
PdS_2	square planar	$Pbca$	5.460	5.541	7.531

2.2. Supercell Surface Models. Slabs cut from the bulk structures have been used to model the 4d TMS surfaces. To better understand the importance of the electronic properties of CUSs, we have chosen surfaces with lowest-index planes that expose coordinatively unsaturated metal atoms. Due to the crystal structure characteristics of the TMS bulk, in some cases CUS sulfur atoms also occupy surface sites. Ab initio molecular dynamics simulations have shown that, under the usual temperatures of an HDS reaction, the average bond lengths at as-cleaved edge surfaces of MoS_2 are only slightly changed with respect to the bulk sulfide.[20] The structure of the RuS_2(100) surface has been experimentally studied by low-energy electron diffraction and scanning tunneling microscopy.[21] This study concluded that after cleavage the surface is unreconstructed and stable. Several tests for the unrelaxed and relaxed surfaces of NbS (not reported here) suggest that for these materials the calculated partial DOS for the unrelaxed and relaxed surface are almost the same.

Periodic boundary conditions for slabs have been imposed by means of the supercell approach (Figure 2). The slabs are perpendicularly separated by a vacuum space of around 10 Å. For NbS and NbS_2 (Figures 2a and 2b), the surface-modeling slabs are composed of four blocks of transition metal atoms alternating with the other four blocks of sulfur atoms in an MSMSMS stacking, where M represents a metal atom. For NbS and NbS_2, the exposed metal atoms correspond to a cleavage at the (0001) and (10$\bar{1}$0) planes (using the four-figure Miller−Bravais notation for hexagonal lattices), respectively. Correspondingly, MoS_2 slabs were constructed for the (10$\bar{1}$0) plane (Figure 2c) given that this is perpendicular to the layered structure of this compound. Nonetheless, due to the different layer-stacking sequence in these sulfides, the NbS_2(10$\bar{1}$0) plane

HDS of 4d-Transition-Metal Sulfides

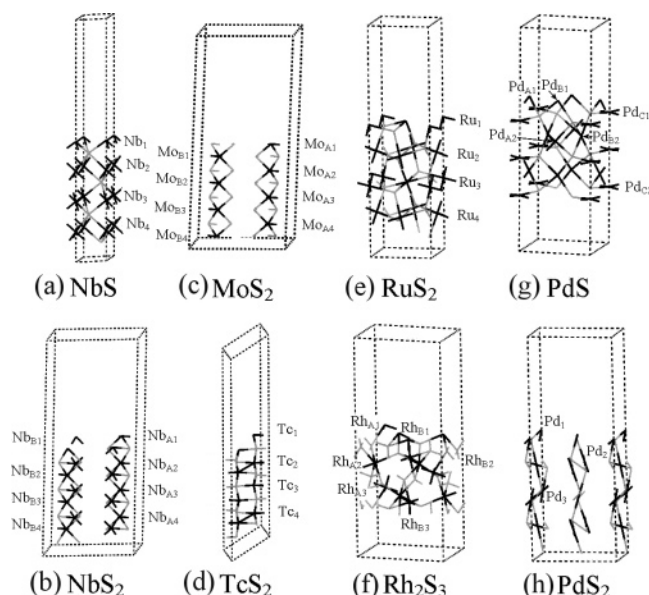*J. Phys. Chem. B, Vol. 110, No. 15, 2006* **7953**

Figure 2. Supercell models used to study the electronic properties of exposed transition metal surface atoms. Dark and light lines represent metal and sulfur atoms, respectively.

does only expose metal atoms while the MoS_2 one exposes alternatively rows of Mo atoms and double rows of S atoms. In the case of TcS_2 and RuS_2 slabs (Figures 2d and 2e, respectively), the chalcogen blocks are composed of sulfur double blocks; hence their block arrangement is MSSMSSMSSMSS. The TcS_2 slab is composed of the Tc atoms nearest to the plane (100) (using the three-figure Miller indexes for a general lattice). As in the case of NbS_2 and MoS_2, this plane is perpendicular to the sulfur−metal−sulfur layers. The metal-exposing surface of the RuS_2 slab is the (001) plane of the pyrite lattice. The chalcogen blocks of the Rh_2S_3 slab are actually sulfur triblocks (Figure 2f). Due to the relatively large chalcogen-block width, only three metal blocks have been considered for this case; i.e., the slab can be schematically represented by MSSSMSSSMSSS. The PdS slab was built with metal blocks separated by other blocks of almost one atom width that contain both metal and chalcogen atoms (Figure 2g). The slab model has three metal blocks alternating with three metal−chalcogen blocks. The metal-exposing face coincides with the (001) plane of the bulk structure. Finally, the stacking of the PdS_2 slab is represented by MSSMSSMSSMSS (Figure 2h), with the (100) plane perpendicular to the layered structure being the one with the exposed metal atoms.

2.3. Computational Procedures. First principles calculations for electronic properties of bulk and surfaces of 4d TMSs were performed using the periodic plane-wave pseudopotential technique as implemented in the CASTEP software package.[22] The exchange−correlation energy has been computed using the revised Perdew−Burke−Ernzerhof (RPBE) implementation[23] of the generalized gradient approximation (GGA) exchange correlation functional, designed to improve the determination of adsorption energies of molecules on metallic surfaces. Ultrasoft pseudopotentials[24] were employed with a plane-wave cutoff energy at least of 290 eV and Monkhorst−Pack k-point grid density $N_A \times N_B \times N_C$ as specified in Table 2. The self-consistent total energies were obtained by the density mixing scheme.[25]

First of all, cluster model calculations on representative 4d TMSs were carried out to investigate the character of the corresponding molecular orbitals (as seen in section 3.1). This set of calculations was carried out using the DMol3 module of the Cerius2 package.[26]

TABLE 2: k-Point Grids Used for RPBE Calculations of Bulk and Surface 4d TMSs

compound	bulk	surface
NbS	$8 \times 8 \times 4$	$12 \times 12 \times 1$
NbS_2	$8 \times 8 \times 2$	$1 \times 10 \times 3$
MoS_2	$8 \times 8 \times 2$	$1 \times 12 \times 3$
TcS_2	$7 \times 8 \times 7$	$1 \times 10 \times 8$
RuS_2	$8 \times 8 \times 8$	$10 \times 10 \times 1$
Rh_2S_3	$6 \times 8 \times 8$	$6 \times 1 \times 8$
PdS	$8 \times 8 \times 8$	$8 \times 8 \times 1$
PdS_2	$8 \times 8 \times 6$	$1 \times 12 \times 9$

To investigate the nature of the chemical bond in these compounds we rely on the net charges obtained through a Mulliken analysis. This technique is known to provide qualitative information and, in particular, to predict the correct trends along a series of similar compounds[27] even if absolute values of charges are generally less reliable.[28,29] Here, it is worth pointing out that because of the use of a plane-wave basis set it is necessary to carry out a projection of the plane-wave states into a localized basis set that is subsequently used to perform the population analysis in bulk systems.[30,31]

3. Results and Discussion

To have a comprehensible picture of the electronic properties of both bulk and surface models, we first comment on the molecular orbitals of these systems as obtained for three cluster models of representative 4d TMSs: RuS_6, MoS_6, and PdS_4.
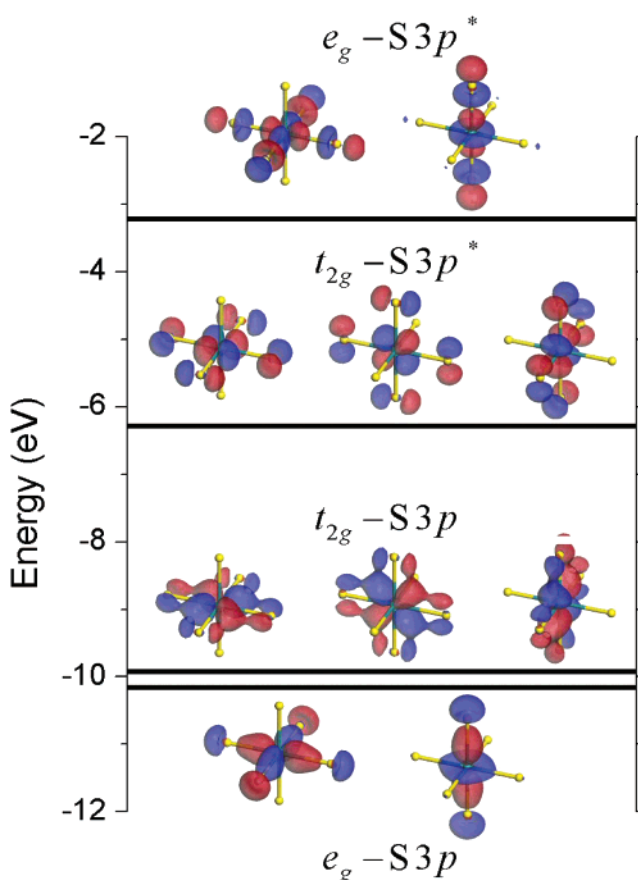

Figure 3. Molecular orbitals and associated energy levels generated by splitting of transition metal d states in octahedral sulfur coordination. The isosurface orbitals shown are for a neutral RuS_6 cluster. Red and blue isosurfaces indicate positive and negative values of the resulting orbitals, respectively. These orbital representations clearly show the mixing between pure d atomic e_g and t_{2g} transition metal orbitals and the sulfur 3p ones to form low-energy bonding (e_g−S3p, t_{2g}−S3p) and high-energy antibonding (e_g−S3p*, t_{2g}−S3p*) molecular orbitals.
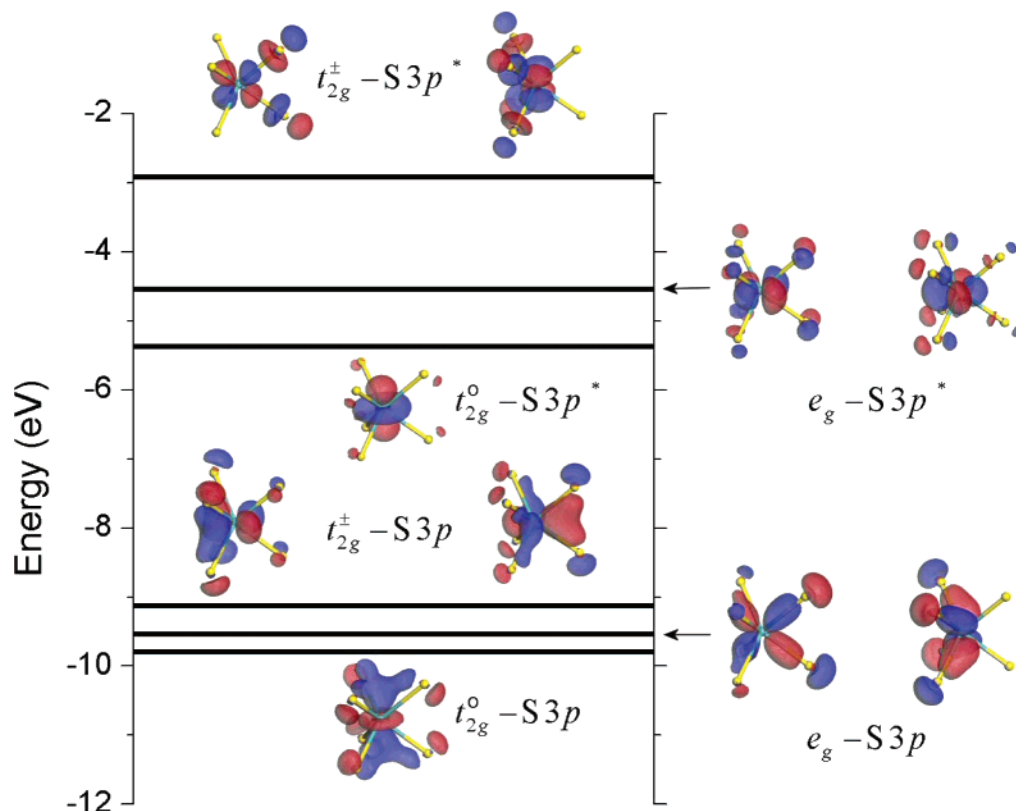
Figure 4. Molecular orbitals and energy levels resulting from splitting of transition metal d orbitals in a trigonal-prismatic coordination of a neutral MoS_6 cluster. The t_{2g}^o, $t_{2g}^\pm$, and e_g orbitals mix with the sulfur 3p ones resulting in low-energy bonding (t_{2g}^o−S3p, e_g−S3p*, $t_{2g}^\pm$−S3p) and high-energy antibonding (t_{2g}^o−S3p*, e_g−S3p*, $t_{2g}^\pm$−S3p*) molecular orbitals.
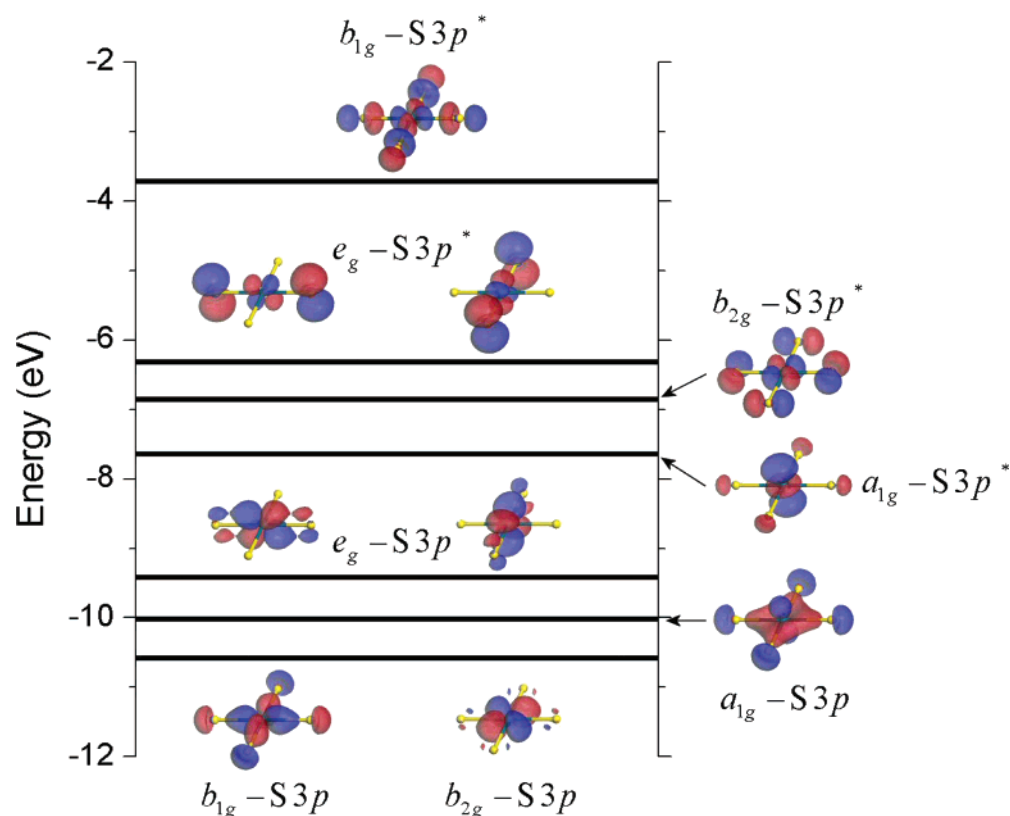

Figure 5. Molecular orbitals and energy levels arising from the splitting of transition metal d orbitals in a square-planar sulfur coordination for the neutral PdS_4 cluster. The b_{1g}, b_{2g}, a_{1g}, and e_g transition metal orbitals hybridize with the sulfur 3p ones to form low-energy bonding (b_{1g}−S3p, b_{2g}−S3p, a_{1g}−S3p, e_g−S3p) and high-energy antibonding (b_{1g}−S3p*, b_{2g}−S3p*, a_{1g}−S3p*, e_g−S3p*) molecular orbitals.

These have octahedral (Figure 3), trigonal-prismatic (Figure 4), and square-planar (Figure 5) coordination around the transition metal site, respectively. Coordination produces d level splitting that is usually explained in terms of the ligand-field theory; this

HDS of 4d-Transition-Metal Sulfides

J. Phys. Chem. B, Vol. 110, No. 15, 2006 **7955**

TABLE 3: Ligand-Field Splitting of d Transition Metal Orbitals

coordination	orbital manifold	degeneration	involved d levels
octahedral	t_{2g}	3-fold	d_{xy}, d_{yz}, d_{xz}
	e_g	2-fold	$d_{x^2-y^2}, d_{z^2}$
trigonal prismatic	t_{2g}°	nondegenerate	d_{z^2}
	$t_{2g}^{\pm}$	2-fold	$d_{xy}, d_{x^2-y^2}$
	e_g	2-fold	d_{yz}, d_{xz}
square planar	e_g	2-fold	d_{yz}, d_{xz}
	b_{1g}	nondegenerate	$d_{x^2-y^2}$
	b_{2g}	nondegenerate	d_{xy}
	a_{1g}	nondegenerate	d_{x^2}

TABLE 4: Energy Levels of the States Resulting from Hybridization between Transition Metal 4d and Sulfur 3p Atomic Orbitals for Cluster Models of Different Sulfur Coordination Symmetries

sulfur coordination	4d metal orbitals	energy level (eV)	
		bonding	antibonding
octahedral (RuS_6)	e_g	−10.154	−3.219
	t_{2g}	−9.920	−6.278
trigonal prismatic (MoS_6)	t_{2g}°	−9.790	−5.370
	$t_{2g}^{\pm}$	−9.124	−4.537
	e_g	−9.531	−2.920
square planar (PdS_4)	b_{1g}	−10.578	−3.712
	b_{2g}	−10.575	−6.857
	a_{1g}	−10.018	−7.637
	e_g	−9.420	−6.311

is to rely mainly on symmetry and Madelung field effects. So, as is shown in Table 3, for the above coordinations it is considered that the ligand field splits the 5-fold d levels into two or more of either 2-fold, 3-fold, or nondegenerate manifolds.[32,33] However, this simplified picture neglects important quantum chemical aspects of these orbitals ignoring their nonbonding, bonding, or antibonding character.

3.1. Cluster Model Analysis of Relevant TMS Orbitals. From Figure 3, it can be appreciated that the t_{2g} orbitals are oriented away from the metal−sulfur bonding directions; thus, they seem to be poorly hybridized with the sulfur p states, as such they have been usually considered as essentially nonbonding orbitals. As well, the e_g orbitals extend along the direction of the metal−sulfur bonds and in that case strongly mix with the sulfur p states. However, these two hybridizations are large enough to rouse a splitting of the purely atomic t_{2g} and e_g orbitals into low-energy bonding and high-energy antibonding states. Thus, because of the strong effect of the metallic atom coordination by sulfur, the split of the transition metal d orbitals

results from both ligand-field and quantum interactions. In this paper we will denote the bonding hybridization between t_{2g} (e_g) and sulfur 3p orbitals by t_{2g}−S3p (e_g−S3p) and the antibonding ones by t_{2g}−S3p* (e_g−S3p*). Table 4 reports the energy levels for some of the one-electron states of the octahedral cluster model and also of the other two cluster models studied here.

Figure 4 shows the bonding and antibonding combinations of the metal 4d and sulfur 3p orbitals, for the trigonal-prismatic coordination case. Due to the fact that the axial direction of t_{2g}° does not contain sulfur atoms, it is generally argued that its molecular orbitals have some nonbonding character; however, Figure 4 and Table 4 indicate that, at least in the cluster model, this picture is not correct.

For the case of the square-planar coordination (Figure 5), the lowest sulfur coordination number (relative to the octahedral or trigonal-prismatic cases) removes the degeneration, and in fact, as we will see below, this occurs also for the exposed transition metal atoms on a sulfide surface. Figure 5 indicates the notation used in this paper for the bonding and antibonding hybridization of metal 4d orbitals with the sulfur 3p ones under present coordination. Note that bonding b_{1g}−S3p and b_{2g}−S3p hybrids are not degenerate (Table 4), as it could be inferred by looking at Figure 5.

3.2. Electronic Structure of Bulk 4d TMSs. The structure of the DOS of the bulk and surface 4d TMSs can be understood in terms of the orbitals obtained for the different coordinations in cluster models shown above. The formation of bonding−antibonding gaps between hybrids of metal 4d and sulfur 3p states due to the ligand-field and covalent bonding interactions between transition metal and sulfur centers is the characteristic feature.

Figure 6 shows the total DOS per atom for the bulk 4d TMS experimental structures listed in Table 1. These sulfides have predominantly semiconductor characteristics except for NbS and NbS_2, which are metallic. The semiconducting 4d TMSs−RuS_2, Rh_2S_3, PdS, and MoS_2−are among the most HDS-active TMSs. However, the band gap width is not a good descriptor to predict the relative HDS activity of sulfides.[13] In general, surfaces of semiconducting lattices obtained by cleavage exhibit new energy levels within the band gap precisely due to the creation of CUSs. Accordingly, the resulting surfaces exhibit a metallic character. Therefore, to elucidate the role of metallic surfaces in the HDS activity appears as necessary. This analysis will complement the insights coming from semiconducting properties of the bulk materials.

To clarify the electronic structure of bulk 4d TMSs, the orbital symmetry of valence states is shown in Figure 7. The projection of DOS onto transition metal d and sulfur p orbitals is shown in Figure 9. In all cases, the valence electrons of the constituent atoms lie within the $-17 < E < -11$ or $-9 < E < 0$ energy
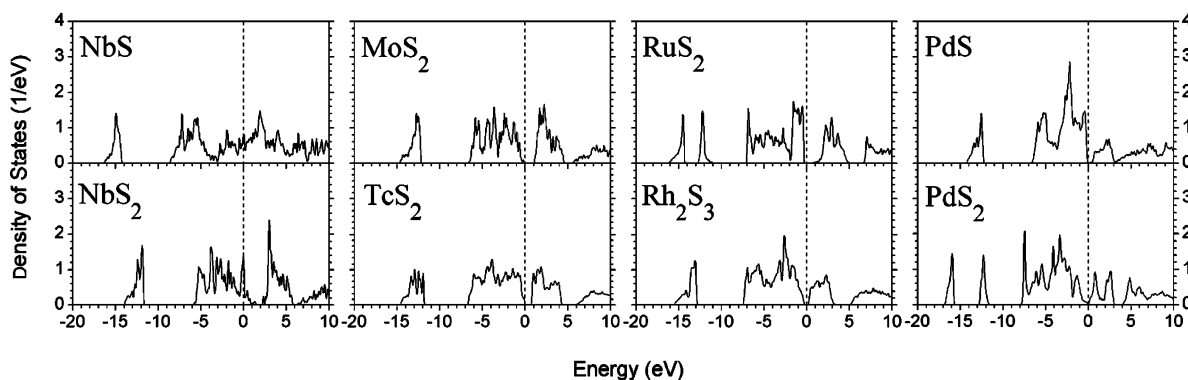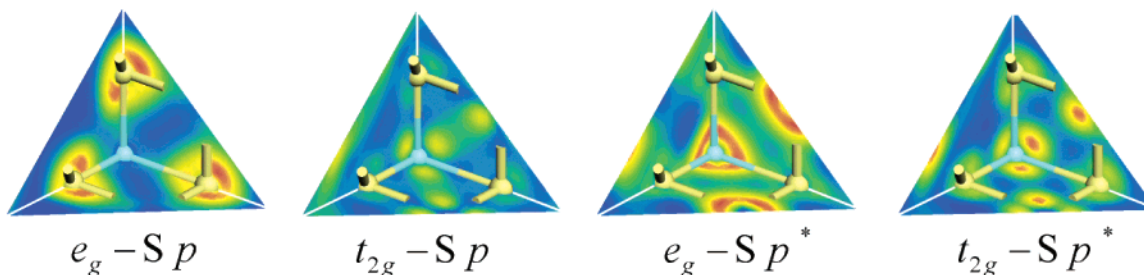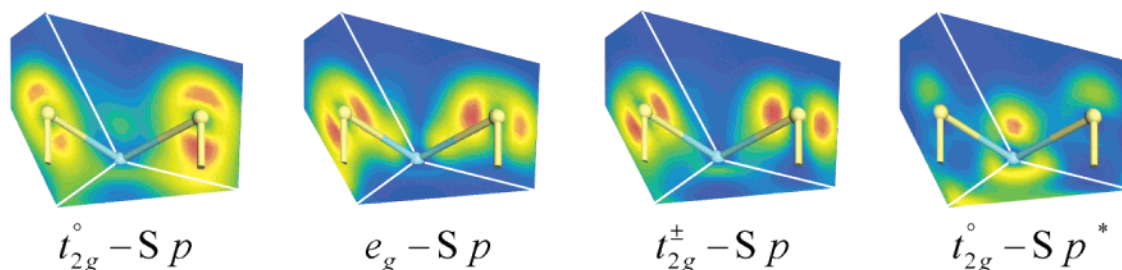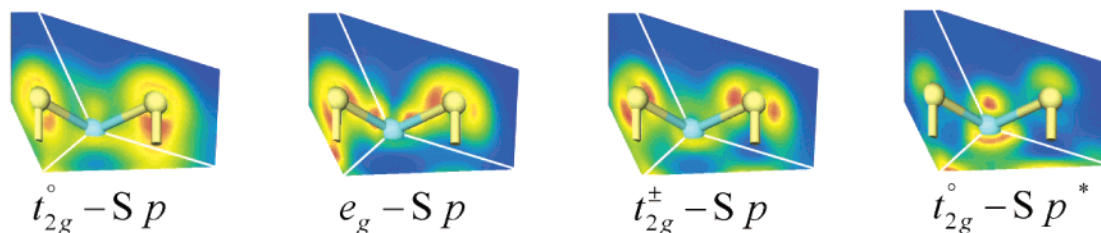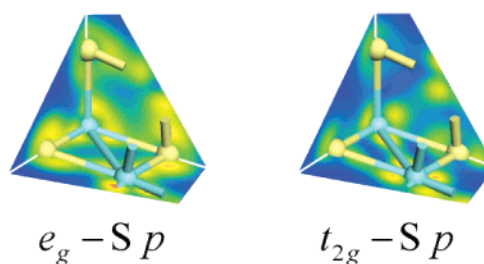

Figure 6. Total DOS per atom for bulk sulfides. Dashed lines indicate the position of the Fermi level. The smearing width used to plot the DOS was 0.05 eV.
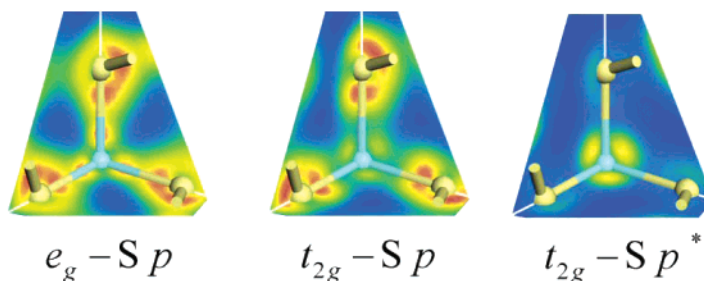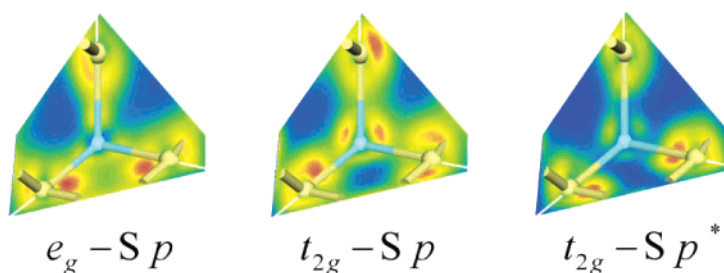
(a) NbS

$e_g - S\,p$ $t_{2g} - S\,p$ $e_g - S\,p^*$ $t_{2g} - S\,p^*$

(b) NbS$_2$

$t_{2g}^{\circ} - S\,p$ $e_g - S\,p$ $t_{2g}^{\pm} - S\,p$ $t_{2g}^{\circ} - S\,p^*$

(c) MoS$_2$

$t_{2g}^{\circ} - S\,p$ $e_g - S\,p$ $t_{2g}^{\pm} - S\,p$ $t_{2g}^{\circ} - S\,p^*$

(d) TcS$_2$

$e_g - S\,p$ $t_{2g} - S\,p$

intervals (in eV). The first one is formed mainly by sulfur 3s states and the second by hybridization of transition metal 4d states with sulfur 3p states. For RuS_2 and PdS_2 compounds, the energy interval containing sulfur s states splits into low-energy bonding σ and high-energy antibonding σ^* states. For most of the 4d bulk sulfides, the energy interval containing both sulfur 3p and transition metal 4d states has also a marked bonding–antibonding splitting, which gives rise to the semiconductor behavior and reveals a strong covalent character of the metal–sulfur bond. This is indeed the reason that simple ligand-field arguments are not enough to describe the nature of the electronic structure of these compounds. The Mulliken-population analysis reported in Table 5 provides qualitative information about the

bonding character and reinforces the above argument. With respect to their covalent character, the 4d TMSs studied in the present work can be ordered as $PdS > Rh_2S_3 > PdS_2 > RuS_2 > TcS_2 \approx MoS_2 > NbS > NbS_2$. For a better comparison of covalence in TcS_2 it is useful to consider the average charge on metal and chalcogen sites ($0.13e$ and $-0.07e$, respectively). Note that, according to the Mulliken analysis, RuS_2 is the only sulfide having negative charge at all of its metal sites. This can be interpreted from the noticeable semiconducting character of RuS_2 (Figure 6), which leads to a filling of the Ru d states.

The valence orbital densities for bulk sulfides (Figure 7) can be compared with those of the sulfide-cluster cases displayed in Figures 3–5. For a periodic system, orbital densities can be
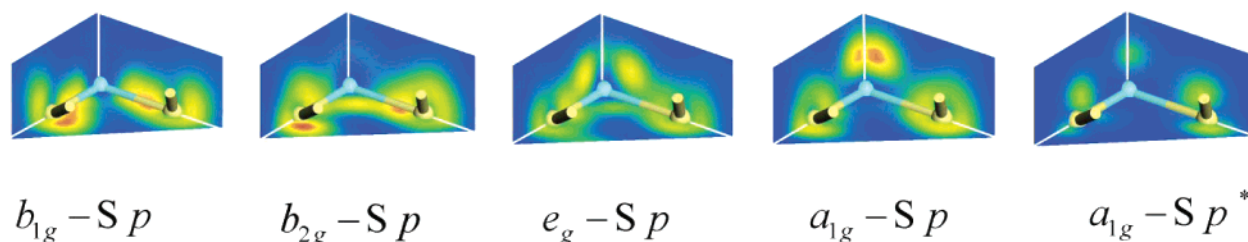
HDS of 4d-Transition-Metal Sulfides

J. Phys. Chem. B, Vol. 110, No. 15, 2006 **7957**

(e) RuS$_2$

$e_g - S\,p$ $t_{2g} - S\,p$ $t_{2g} - S\,p^{*}$

(f) Rh$_2$S$_3$

$e_g - S\,p$ $t_{2g} - S\,p$ $t_{2g} - S\,p^{*}$

(g) PdS

$b_{1g} - S\,p$ $a_{1g} - S\,p$ $e_g - S\,p$ $a_{1g} - S\,p^{*}$

(h) PdS$_2$

$b_{1g} - S\,p$ $b_{2g} - S\,p$ $e_g - S\,p$ $a_{1g} - S\,p$ $a_{1g} - S\,p^{*}$

Figure 7. Valence orbital densities for bulk sulfides as resulting from hybridization between sulfur 3p and transition metal 4d states. For simplicity, atoms have been hidden except a (blue) central transition metal atom and its (yellow) ligand sulfur atoms. (a) NbS, (b) NbS$_2$, (c) MoS$_2$, (d) TcS$_2$, (e) RuS$_2$, (f) Rh$_2$S$_3$, (g) PdS, and (h) PdS$_2$.

obtained by taking the square of the absolute value of the one-electron wave function corresponding to a given electronic band (Figure 8) and summing over all points in *k*-space. The color scale in Figure 7 attempts to measure orbital intensities arising from some bands. A rainbow scale is used where blue and red indicate the minimum and maximum intensities, respectively. Table 6 summarizes the energy ranges for the different types of valence orbitals as obtained sfrom our calculations.

In the following, the band structures of the 4d TMSs studied in the present work are discussed in some more extended detail, foc-using especially on the compounds with the highest HDS activity.

3.2.1. NbS. Figure 9a shows the overlap between the S 3p and the Nb 4d states whose highest DOS peaks, positioned at E_{S-p} and E_{Nb-d}, respectively, are separated by $\Delta E_{S-p;Nb-d} \approx 9$ eV. This indicates that NbS has a predominantly ionic bond, which is confirmed by the Mulliken populations (Table 5) and also by Figure 7a, showing that orbitals appear to concentrate most of the density around sulfur atoms for e_g–S3p states and around metal atoms for t_{2g}–S3p, (e_g–S3p)*, and (t_{2g}–S3p)*.

The partial DOS shows that Nb 4d band contributions subdivide into two band regions ranging from $E_1 \approx -9$ to -4 eV and from $E_2 \approx -4$ to 6 eV. The Nb 4d E_1 set hybridizes
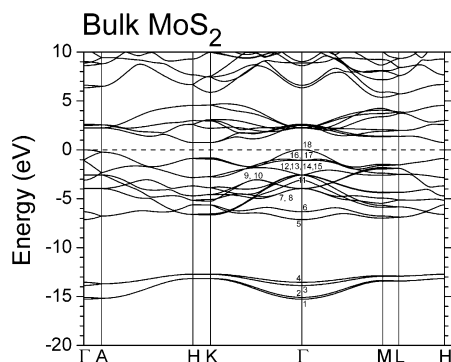
Figure 8. Dispersion relation $E(k)$ for MoS_2. Small numbers next to curves denote band ordering. The projection of bands onto the energy axis gives the energy intervals reported in Table 5. The dashed line indicates the position of the Fermi level.

TABLE 5: Mulliken Atomic Populations for Bulk Sulfides[a]

compound	species	s	p	d	total	charge (e)
NbS	Nb	0.30	0.09	4.36	4.75	0.25
	S	1.82	4.43	0.00	6.25	−0.25
NbS$_2$	Nb	0.36	0.17	4.12	4.66	0.34
	S	1.88	4.29	0.00	6.17	−0.17
MoS$_2$	Mo	0.42	0.18	5.27	5.87	0.13
	S	1.88	4.18	0.00	6.06	−0.06
TcS$_2$	Tc$_1$	0.53	0.17	6.19	6.89	0.11
	Tc$_2$	0.53	0.13	6.18	6.85	0.15
	S$_1$	1.90	4.10	0.00	6.00	0.00
	S$_2$	1.90	4.13	0.00	6.03	−0.03
	S$_3$	1.89	4.19	0.00	6.08	−0.08
	S$_4$	1.88	4.28	0.00	6.16	−0.16
RuS$_2$	Ru	0.36	0.29	7.45	8.09	−0.09
	S	1.82	4.13	0.00	5.95	0.05
Rh$_2$S$_3$	Rh	0.53	0.27	8.16	8.96	0.04
	S	1.83	4.20	0.00	6.03	−0.03
PdS	Pd$_1$	0.55	0.19	9.24	9.98	0.02
	Pd$_2$	0.54	0.26	9.24	10.04	−0.04
	S	1.81	4.17	0.00	5.97	0.03
PdS$_2$	Pd	0.50	0.17	9.27	9.95	0.05
	S	1.86	4.17	0.00	6.03	−0.03

[a] The nonequivalent sites for TcS$_2$ and PdS are those specified in Figure 1.

somewhat with S 3p states; thus the Nb 4d states belonging to this set are mainly e_g−S3p states due to the octahedral sulfur coordination around Nb atoms. A direct visualization of the NbS orbital densities confirms this insight (Figures 7a and 10). As a result of the e_g−S3p hybridization, there must be both bonding low-energy and antibonding high-energy states. An inspection of the DOS for energies higher than approximately −4 eV shows that the S p contribution to the DOS is low. Thus, the absence of a marked splitting in the S p energy is also consistent with a small covalent contribution. Despite the poor contribution of S p states to the DOS in the E_2 interval, Figure 7a shows the existence of some hybridization between them and the Nb d states. Table 6 shows that the bottom region of the E_2 interval is formed by bonding (t_{2g}−S3p) hybrids, whereas the middle region, including the Fermi level ($E = 0$), is formed by both antibonding (e_g−S3p)* and (t_{2g}−S3p)* hybrids. The partial electron occupancy of the E_2 interval is responsible for the metallic character of NbS. For the NbS and NbS$_2$ metallic sulfides it is worth mentioning that charge densities in Figure 7 are used only to find the symmetry of one-electron levels independently of their electron occupancy.

3.2.2. NbS$_2$.. The NbS$_2$ valence band region lies in the energy interval going from approximately −6 eV to the Fermi level. These are clearly formed by hybridization between the Nb d split under the trigonal-prismatic coordination and S p states. This hybridization results in a larger covalent character than that of the NbS. This is clearly seen from both orbitals (Figure 7b) and partial DOS (Figure 9b). The hybridization leads to bonding t_{2g}^o−S3p, e_g−S3p, and $t_{2g}^{\pm}$−S3p orbitals and a half-filled energy interval of antibonding (t_{2g}^o−S3p)* orbitals. The energy intervals for all of these orbitals are reported in Table 6. The areas under the partial DOS graphs going from approximately −6 to −0.5 eV for each Nb d and S p state are roughly the same, with a slightly larger value for the latter, indicating that the bulk metal−sulfur bond in NbS$_2$ is more covalent than that in NbS. The covalent character is confirmed by the existence of an antibonding energy band ranging from ∼2 to 6 eV; this displays a clear mixing between the Nb d and the S p orbitals forming the (e_g−S3p)* states (Figure 11). The shorter distance between nearest transition metal atoms in NbS$_2$ produces a larger splitting in the bonding−antibonding states. The NbS$_2$ Fermi level appears located at the (t_{2g}^o−S3p)* energy band, and this has indeed a sharper DOS than the NbS
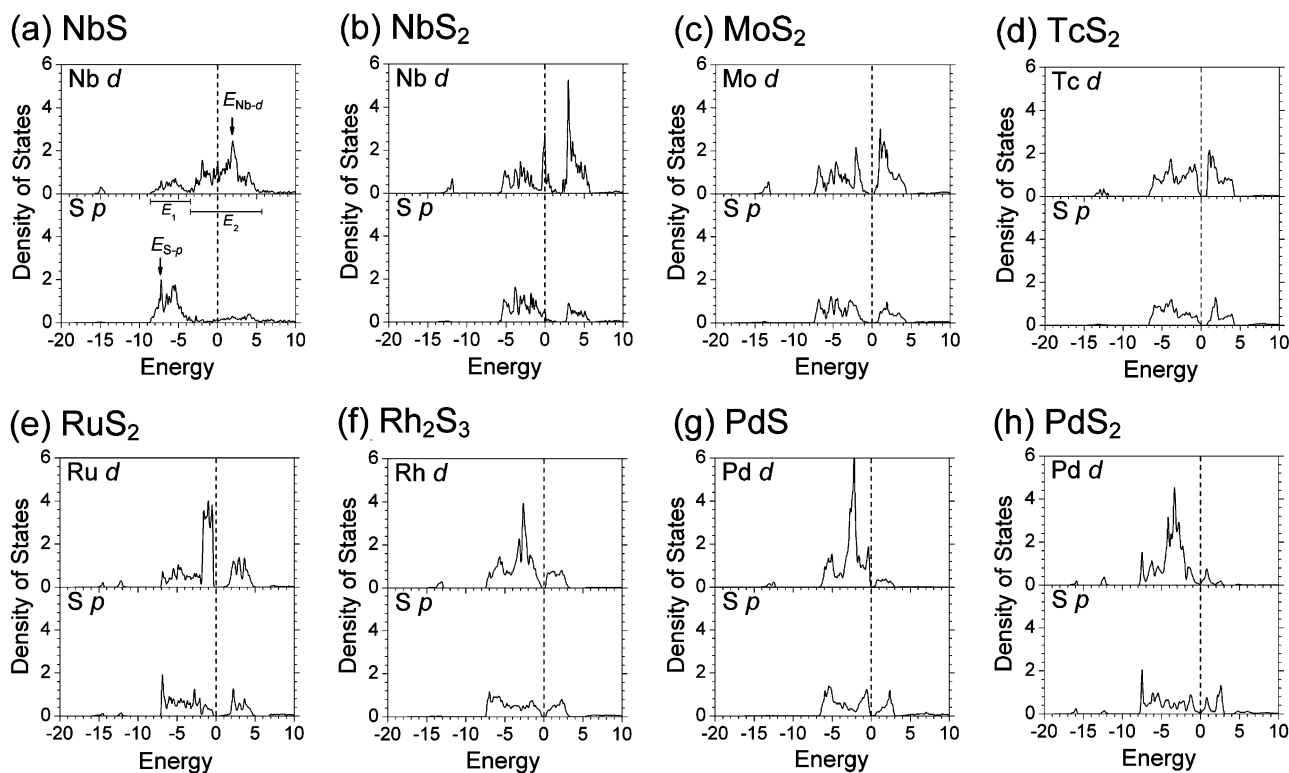
TABLE 6: Valence Band Energy Intervals for Bulk Sulfide Hybrids (in eV)[a]

compound	hybrid type of bulk valence orbitals				
NbS	e_g−S3p −6.88, −4.55	t_{2g}−S3p −3.52, −0.73	(t_{2g}−S3p)* −1.28, 1.06	(e_g−S3p)* −1.10, 1.82	
NbS$_2$	t_{2g}^o −5.74, −4.55	e_g−S3p −4.71, −1.61	$t_{2g}^{\pm}$−S3p −2.79, −1.41	(t_{2g}^o−S3p)* −0.27, 3.97	
MoS$_2$	t_{2g}^o−S3p −6.99, −5.94	**e_g−S3p −6.05, −2.56**	$t_{2g}^{\pm}$−S3p −3.91, −2.33	t_{2g}^o−S3p)* −1.81, 0.00	
TcS$_2$	e_g−S3p −6.48, −2.75	**t_{2g}−S3p −3.01, 0.00**			
RuS$_2$	**e_g−S3p −6.49, −2.20**	t_{2g}−S3p −3.82, −1.80	(t_{2g}−S3p)* −1.59, 0.00		
Rh$_2$S$_3$	e_g−S3p −7.15, −3.63	**t_{2g}−S3p −3.90, −3.51**	(t_{2g}−S3p)* −3.38, 0.00		
PdS	**b_{1g}−S3p −6.48, −4.00**	a_{1g}−S3p −4.30, −2.33	e_g−S3p −2.48, −1.52	(a_{1g}−S3p)* −1.74, 0.00	
PdS$_2$	**b_{1g}−S3p −7.69, −5.31**	b_{2g}−S3p −5.10, −2.69	e_g−S3p −4.60, −2.04	a_{1g}−S3p −2.54, −1.77	(a_{1g}−S3p)* −1.81, 0.00

[a] The boldface type indicates the covalent bands.

Figure 9. Angular-momentum-decomposed DOS per atom for bulk sulfides: (a) NbS, (b) NbS_2, (c) MoS_2, (d) TcS_2, (e) RuS_2, (f) Rh_2S_3, (g) PdS, and (h) PdS_2. Dashed lines indicate the Fermi-energy position. For the NbS case, the DOS maximum positions used to determine the difference $\Delta E_{S-p;Nb-d} = E_{Nb-d} - E_{S-p}$ are indicated with arrows.
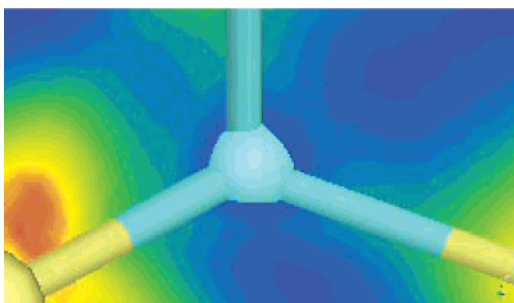

Figure 10. Closer view of the NbS e_g–S3p hybrid density shown in Figure 7a, showing a minor contribution of Nb e_g orbitals. The central blue atom is Nb, whereas the yellow sticks represent bonds to S.
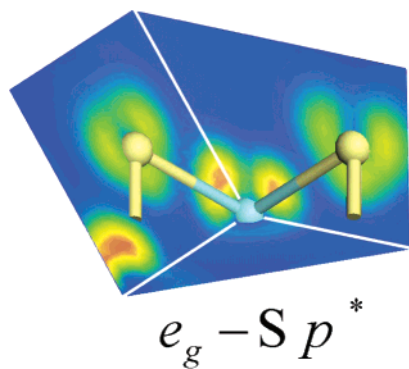

$$e_g - S\,p^*$$

Figure 11. Electron density of unoccupied antibonding states with energy levels from ~2 to 6 eV for NbS_2.

$$e_g - S\,p^*, t_{2g}^\pm - S\,p^*$$

Figure 12. Electron density of MoS_2 unoccupied antibonding hybrid states from ~1 to 4 eV.

3.2.3. MoS$_2$. The crystal structure of MoS_2 suggests that the energy-band structure would be similar to that of NbS_2. In fact, a comparison between their orbitals in Figures 7b and 7c and their DOSs in Figures 9b and 9c confirms this assumption. In MoS_2, the extra valence electrons relative to NbS_2 fully fill the antibonding $(t_{2g}^o - S3p)^*$ band, which is neatly separated from the conduction band. This gives rise to the well-known semiconducting character of bulk MoS_2. From ligand-field arguments one would predict that the nondegenerate transition metal t_{2g}^o orbitals have lower energies than those of the doubly degenerate $t_{2g}^\pm$ and e_g ones. Hence, S 3p orbitals would overlap only with the transition metal t_{2g}^o ones in the valence band while the $t_{2g}^\pm$ and e_g orbitals would develop the lowest group of conduction bands.[7] However, as Figure 7c and Table 6 show, there is a strong covalent bonding hybridization among Mo e_g and S p orbitals in the valence band. Hybridization of S 3p orbitals with Mo $t_{2g}^\pm$ and e_g states leads to bonding $t_{2g}^\pm$–S3p and e_g–S3p states (Figure 7c) in the valence band, whereas ($t_{2g}^\pm$–S3p)* and $(e_g$–S3p)* states appear in the conduction band (Figure 12). Thence, Mo $t_{2g}^\pm$ and e_g orbitals contribute noticeably to states both below and above the Fermi level.

$(e_g$–S3p)* one. Although it appears that the low-energy bonding t_{2g}^o orbitals are essentially S p states with a concomitant almost null hybridization, the importance of orbital mixing can be indirectly inferred from the appearance of its antibonding (t_{2g}^o–S3p)* counterpart at the Fermi level.
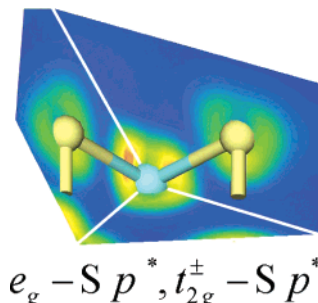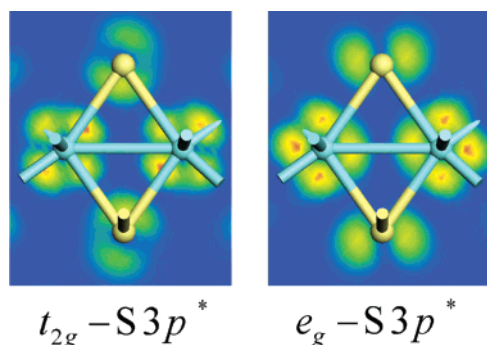
Figure 13. Electron density of unoccupied orbitals of the TcS_2 conduction band on the energy interval between 0.99 and 2.86 eV for $(t_{2g}-S3p)*$ and 2.36 and 4.29 eV for $(e_g-S3p)*$. Slices shown contain sulfur and metal atoms on the plane containing metal-metal bonds.

3.2.4. TcS₂. This disulfide has a layered structure and exhibits semiconducting properties such as MoS_2. However, in this case the sulfur coordination around Tc is octahedral instead of trigonal-prismatic. Its structure is a distorted $Cd(OH)_2$ one with the Tc atoms in each layer forming metal-metal bonds. As a consequence, all d electrons are delocalized over the whole valence band and are strongly hybridized with S 3p states (Figure 9d). Direct counting of bands in the dispersion relation of TcS_2 (not shown here) gives 8 S s lowest bands, 30 valence bands of bonding Tc d-S p hybrids, and 14 conduction bands of antibonding Tc d-S p hybrids. This agrees with the 52 bands provided by the TcS_2 four formula unit cell; each formula unit has 2 S s, 6 S p, and 5 Tc d states. Here, separation among valence e_g-S3p and $t_{2g}-S3p$ hybrids, as seen in the Nb and Mo disulfides, is not visible because of the strong overlap between Tc 4d orbitals due to the rather short Tc-Tc distances. The valence Tc d-S p hybrids are formed by 30 bands of bonding character only (Figure 7d), and its top part, where the Fermi level lies, is composed of $t_{2g}-S3p$ hybrids. The 14 lowest conduction bands are composed of antibonding $(t_{2g}-S3p)*$ and $(e_g-S3p)*$ hybrids (Figure 13). The semiconducting character of TcS_2 arises from the full filling of bonding states, which are well separated from the next antibonding ones. The more uniform valence orbital intensities over metal and chalcogen atoms reveal an increased covalent strength of TcS_2 relative to NbS, NbS_2, and MoS_2.

3.2.5. RuS₂. In the cubic pyrite structure of RuS_2 there are S-S pairs that contribute to the electronic structure by means of diatomic molecular orbitals in the following order: s σ (1 band), s σ* (1 band), p σ (1 band), p π (2 bands), p π* (2 bands), and p σ* (1 band). Sulfur octahedral symmetry around Ru atoms produces the splitting of the d orbitals into t_{2g} (3 bands) and e_g (2 bands) states, which allocate half of the p π* and p σ* states. In an ionic picture, the 20 available valence electrons per formula unit completely fill states from S s σ to Ru t_{2g} thus leading to a gap between t_{2g} and e_g bands. Clearly, this picture is oversimplified since it ignores the existence of hybridization between orbitals of sulfur dimers and ruthenium atoms (Figures 7e and 14), giving rise to the corresponding bonding and antibonding combinations. However, while the ionic picture explains the RuS_2 semiconducting character, it does not give any clue to the origin of its good HDS activity, which rather is a consequence of covalent interactions.

Figure 15 reports the energy-band structure of this compound. Since there are 80 valence electrons in the unit cell of RuS_2, the valence band region is composed by 40 bands. Notice that the counting of bands is easier over *k*-point intervals XR or RM, where curves are 2-fold and 4-fold degenerate, respectively.
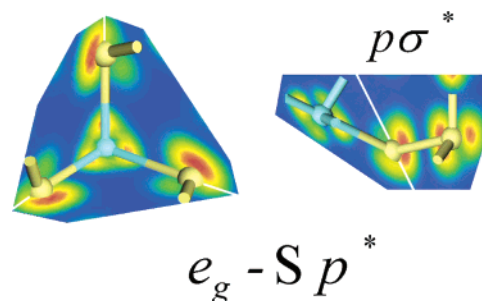

Figure 14. Electron density of the unoccupied antibonding $(e_g-S3p)*$ hybrid states of RuS_2 between ~1.5 and 5 eV. The slice view is centered at an Ru atom (left picture) and an S atom (right picture). The sulfur dimer orbital participating in the hybrid is a p σ* molecular state.
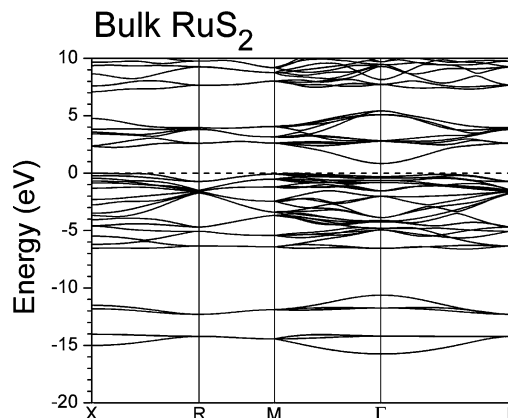

Figure 15. Dispersion relation *E*(*k*) for RuS_2. There are 40 valence bands in the approximately -16-0 eV energy range.

For each valence band, Figure 16 shows the hybridization between S 3p and Ru d states. Table 7 specifies the number of valence electrons participating in each hybrid. This information together with Figure 7e and Table 6 reveals that in the energy range from -6.5 to -2 eV there is a strong covalent interaction between Ru and S leading to e_g-Sp hybrids. This is in clear contrast with a purely ionic picture where only e_g contributions would appear in the conduction band. In addition, in the approximately -4 to -2 eV region Ru $t_{2g}-S3p$ bonding hybrids appear that result from the interaction between Ru t_{2g} orbitals and sulfur 3p orbitals. Similarly, antibonding $(t_{2g}-S3p)*$ states appear in the approximately -1.6-0 eV energy range. From Figures 7e and 15 it would appear that levels 29-40 (Figure 16) have no sulfur contributions. However, the DOS represented in Figure 9e clearly shows their participation albeit with a very low weight. Thus, at the Fermi level of bulk RuS_2 electron states are mainly nonbonding hybrids although with some degree of antibonding character.

It is worthy to stress that RuS_2 is the only sulfide exhibiting total negative charges over all metal atoms (Table 5). Obviously, that is false; this is due to the fact that we are using Mulliken-population analysis. What one should understand is that Ru in this sulfide is not as positive as all of the other transition metal atoms. This can be rationalized from Table 7 as follows: The valence antibonding S_2 molecular states keep charge density away from the neighboring sulfur atoms with a concomitant electronic transfer to Ru atoms, in such a way generating negative charges on metal sites in the Mulliken-population analysis. Thus, present negative charges must be interpreted only as a support that the high HDS activity of RuS_2 can be related to the induced electron-acceptor character of Ru metal sites. Additionally, in connection with the theoretical approach used in this work, a plane wave with a pseudopotential allows a 5p
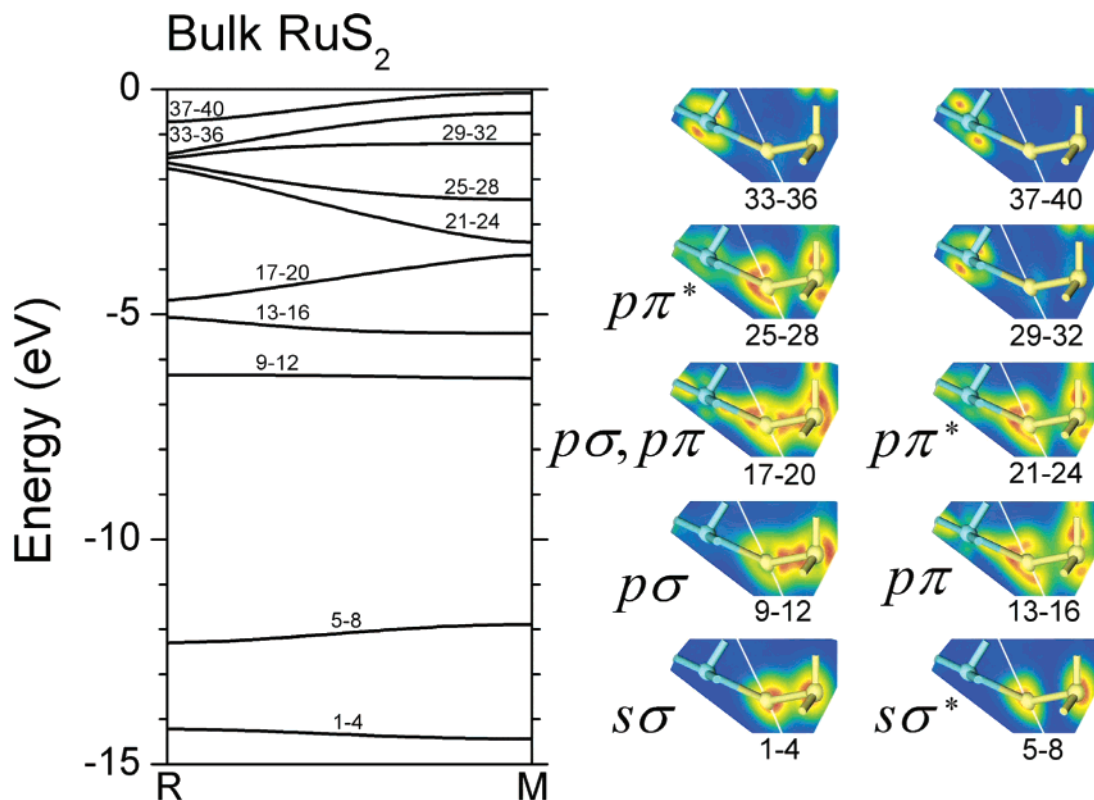
HDS of 4d-Transition-Metal Sulfides

J. Phys. Chem. B, Vol. 110, No. 15, 2006 **7961**

Figure 16. Left: Counting of valence bands for the dispersion relation of RuS_2 on the RM k-point interval. Right: Electron density slices showing S_2 contributions to hybridization for each valence band set.

TABLE 7: Filling of the 40 Bands Constituting the Valence States of RuS_2[a]

bands	hybridization	number of electrons per unit cell
1−4	S s σ	8
5−8	S s σ*	8
9−12	Ru e_g−Spσ	8
13−16	Ru e_g−Spπ	8
17−20	Ru e_g−Spσ Ru e_g−Spπ	8
21−24	Ru e_g−Spπ*	8
25−28	Ru t_{2g}−Spπ*	8
29−40	(Ru t_{2g}−Spσ)*	24
41−52	(Ru e_g−Spσ)*	24 (empty bands)

[a] The last row shows available states at the lowest conduction band.

diffuse orbital, included in the current Ru potential, to allocate extra electron density.

3.2.6. Rh_2S_3. Hybridization among Rh d and S p states occurs on the energy-band region from approximately −7.2 to 0 eV (Table 6). The covalent bond is essentially the result of the bonding t_{2g}−S3p states in the [−4, −3.5] eV energy range. From approximately −3.4 to the Fermi level, the orbital character changes to antibonding (t_{2g}−S3p)*. The dispersion relation for Rh_2S_3 (not shown here) reveals that the four formula units per cell give 88 bands distributed among the valence and conduction bands as follows: 12 S s levels, 26 bands for e_g−S3p hybrids, 34 bands for t_{2g}−S3p hybrids, all these in the valence region, and 16 bands for the conduction (e_g−S3p)* hybrids.

3.2.7. PdS. The sulfur square-planar coordination around Pd atoms concentrates almost all of the Pd d states below the Fermi level (Figure 9g). The prominent peak of Pd d contribution along the −4.3−1.5 eV interval to the DOS indicates an increased ionic character. This energy interval contains contributions from a_{1g}−S3p and e_g−S3p states (Table 6). Orbitals just at the Fermi

level are antibonding (a_{1g}−S3p)* hybrids that occupy an energy interval from approximately −1.8 eV to the Fermi level.

3.2.8. PdS_2. The bulk DOS of PdS_2 has similarities with those of PdS and RuS_2 because of the square-planar coordination (PdS) and the modified pyrite structure (RuS_2). Pd d−S p hybridization takes place in the energy-band region from approximately −7.8 to 0 eV. The orbital intensities reveal the larger ionic character of PdS_2 relative to PdS. The orbitals at the Fermi level are antibonding (a_{1g}−S3p)*.

3.3. Electronic Structure of 4d TMS Surfaces. To investigate the possible influence of CUSs in the HDS activity it seems necessary to analyze the changes of electronic properties of the transition metal atoms in going from the bulk to the surface. Hence, the local DOS at metal sites for the slabs modeling the different sulfur coordinations are shown in Figures 17−24. The slab models are thick enough so that the local DOS of the most inner atoms reproduces the main characteristics of the corresponding bulk metal and chalcogen ones. In general, when compared to the bulk, the surface-exposed-metal-atom local DOS increases around the Fermi level due to the creation of surface states (Table 8). Changes in the electronic structure of the S atoms near the surface relative to the bulk ones are small. This is of course because the present surface models are metal-terminated. One must recall that these surfaces are not necessarily the most stable ones and they are used only as a suitable model to investigate the electronic-structure changes indicated above. For simplicity, hereafter the label "S3p" from the notation of hybrids will be omitted.

3.3.1. NbS(0001). Figures 17 and 25a and Table 8 show that, compared to the bulk (Figure 9a), on the NbS(0001) surface the increment of local DOS below the Fermi level at the exposed Nb atom (labeled as "Nb₁") comes from t_{2g}^* states located in a band range between approximately −0.7 and 0 eV. The sharpness of this peak indicates an acquired nonbonding nature.

TABLE 8: Energy Intervals (in eV) for Surface States near the Fermi Level on Exposed Metal Atoms
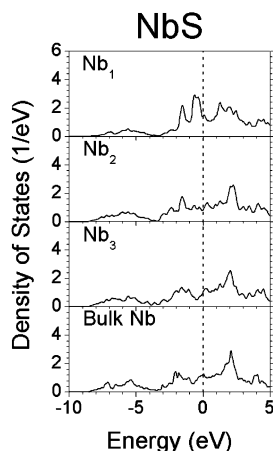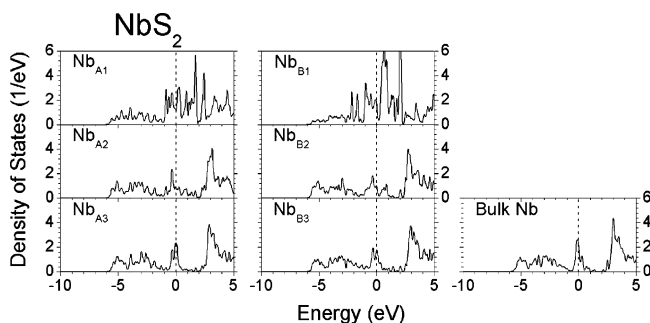
compound	hybrid type of surface orbitals				
NbS	d_{z^2} −1.6, −0.78	t_{2g}^* −0.67, −0.03	$d_{z^2}^*$ −0.21, 1.74		
NbS$_2$	d_{xy}, t_{2g}° −0.78, −0.43	d_{xy}, t_{2g}° −0.18, −0.02	$d_{x^2-y^2}^*, t_{2g}^\pm$ −0.06, 0.23	$d_{x^2-y^2}^*, d_{yz}^*$ 0.03, 0.40	d_{xz}^*, d_{xy}^* 0.19, 0.56
MoS$_2$	d_{xz}^* −0.76, −0.32	d_{yz}^* −0.17, 0.00	$d_{x^2-y^2}^*$ 0.10, 0.64	d_{yz}^* 0.12, 0.83	
TcS$_2$	d_{xz} −0.45, −0.38	d_{yz} −0.33, 0.00	d_{xy}^* 0.23, 0.37	d_{xz}^* 0.23, 0.32	
RuS$_2$	t_{2g}^* −0.83, 0.00	$d_{z^2}^*$ 0.34, 0.95			
Rh$_2$S$_3$	t_{2g}^* −1.55, −1.11	e_g^* −0.45, 0.62			
PdS	$d_{z^2}^*$ −1.39, −1.01	$d_{x^2-y^2}^*$ −0.31, 1.02			
PdS$_2$	$d_{z^2}^*$ −1.77, −1.49	sulfur p_z −0.54, 0.12	$d_{x^2-y^2}^*$ 0.00, 0.49		

In the approximately −0.2−1.7 eV range there is a band region formed mainly by antibonding $d_{z^2}^*$, which comes from the breaking of degeneration in the bulk e_g^* states and a mixture of the t_{2g}^* ones. This suggests a lower HDS activity compared with that of RuS$_2$ as discussed below.

3.3.2. NbS$_2$(10$\bar{1}$0). In the NbS$_2$(10$\bar{1}$0) slab model, there are two layers exposing metal atoms that are denoted as "Nb$_{A1}$" and "Nb$_{B1}$" (Figure 2b). At both exposed Nb$_{A1}$ and Nb$_{B1}$ atoms, the local DOS around the Fermi level increases due to the weakening of the bonding−antibonding separation in the hybridized e_g states (Figures 18 and 25b and Table 8). Although the bulk NbS$_2$ Fermi level coincides with the position of the $t_{2g}^{\circ*}$ peak maximum, at surface metal atoms this maximum is pushed out from the Fermi level by the displacement of the neighboring e_g states, leading to a decrease of the local DOS at the Fermi level. Moreover, the bonding and antibonding hybrids of e_g and t_{2g}° orbitals, located both just above and below the Fermi level, present some nonbonding character. This could be favorable for the HDS activity in an NbS$_2$ surface relative to that of an NbS one, which has nonbonding states only below the Fermi level.

3.3.3. MoS$_2$(10$\bar{1}$0). The MoS$_2$(10$\bar{1}$0) surface, which is considered to be chemically reactive for MoS$_2$,[34,35] exposes rows of coordinatively unsaturated S and Mo atoms in alternating S−Mo−S layers, in contrast to the NbS$_2$(10$\bar{1}$0) surface that exposes unsaturated metal atoms only. The local DOS analysis of the nonrelaxed surface (Figure 19) is in agreement with that

reported for the relaxed surface[20] as already discussed in section 2.2. At the Fermi level, the local DOS of exposed Mo atoms, labeled as "Mo$_{A1}$" (Figure 2c), is noticeably different from zero. Thus, the surface becomes metallic because of upward shift of the bulk $t_{2g}^{\circ*}$, which becomes closer to the Fermi level. Also, some of the antibonding e_g^* conduction states move downward (Figures 19 and 25c and Table 8), resulting in a whole contribution to the bulk gap states. The Mo$_{A1}$-atom-related peak below the Fermi level and located in the interval [−0.8, −0.3] eV is formed by antibonding d_{xy}^* states, which in the bulk sulfide were mainly of $t_{2g}^{\pm}$* character. Just at the Fermi level, the states have antibonding d_{xy}^* hybrid character (formerly in the bulk case of e_g symmetry), although the surface states are mainly localized on the sulfur atoms. Above the Fermi level, the surface states appear to be more intense on the Mo atoms than on the S ones. In fact, one may notice that at the Fermi level the Mo$_{A1}$ local DOS has a positive slope. Hence, the MoS$_2$-

Figure 18. Local DOS for transition metal atoms in the NbS$_2$(10$\bar{1}$0) slab model.

Figure 17. Evolution of local DOS for transition metal atoms from surface to bulk positions in the NbS(0001) slab model.
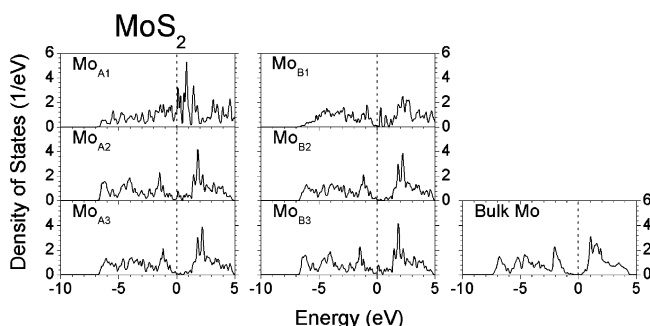
Figure 19. Local DOS for transition metal atoms in the MoS$_2$(10$\bar{1}$0) slab model.

HDS of 4d-Transition-Metal Sulfides

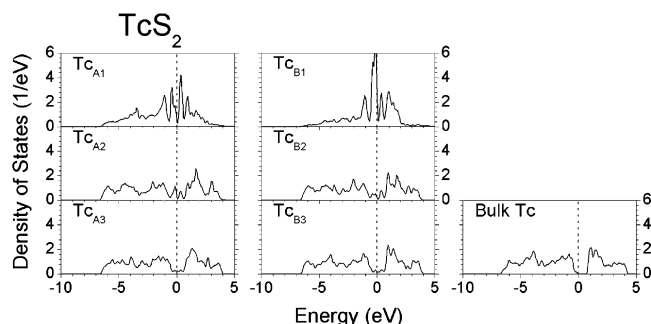*J. Phys. Chem. B, Vol. 110, No. 15, 2006* **7963**

Figure 20. Local DOS for transition metal atoms in the slab model of TcS$_2$.

Figure 22. Local DOS for transition metal atoms in the slab model of Rh$_2$S$_3$.
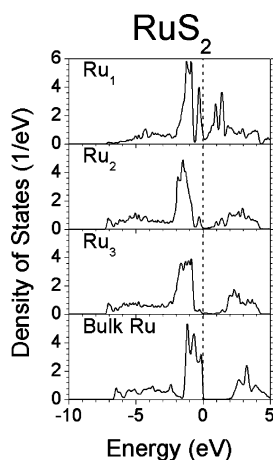
Figure 21. Local DOS for transition metal atoms in the slab model of RuS$_2$.

Figure 23. Local DOS for transition metal atoms in the slab model of PdS.

Figure 24. Local DOS for transition metal atoms in the slab model of PdS$_2$.

(10$\bar{1}$0) surface could facilitate the electron donation step from the organosulfur molecules to the exposed catalyst metal, but it possibly has difficulties in the back-donation step. Thus, the better HDS performance of MoS$_2$(10$\bar{1}$0) relative to NbS$_2$(10$\bar{1}$0) may be due to the fact that for the latter there are not sufficient available states on the metal active site above the Fermi level. Moreover, it is interesting to note that the nonbonding character of the MoS$_2$(10$\bar{1}$0) surface states around the Fermi level becomes more nonbonding than that in NbS$_2$(10$\bar{1}$0). This nonbonding nature may favor further HDS activity because in the MoS$_2$(10$\bar{1}$0) case the surface orbitals do not imply the catalyst sulfur atoms and hence are free to interact with the hydrocarbon sulfurs instead.

3.3.4. TcS$_2$(001). Similarly to the MoS$_2$(10$\bar{1}$0) case, the surface-metal-site DOS at the Fermi level increases from the bulk DOS zero value (Figure 20). For unsaturated surface Tc atoms the local DOS has a minimum value just at the Fermi level. This could suggest a better HDS activity for TcS$_2$ than for MoS$_2$ because the number of both available electrons to back-donate and virtual states to receive donated electrons increases. The states just below and above the Fermi level, which in bulk sulfide are of t$_{2g}$ symmetry, have mainly d$_{yz}$ and d$_{xy}^*$ hybrid nonbonding character, respectively. This confirms the molecular-based-calculation suggestion that a high catalyst HOMO occupation is related to good HDS performance.[1]

3.3.5. RuS$_2$(001). In the RuS$_2$(001) surface, the loss of octahedral coordination around the exposed Ru atom (denoted with "Ru$_1$") reduces the degree of splitting among the Ru d levels (Figure 21). The narrow peak located in the approximately −0.8−0 eV interval is composed of surface states of the t$_{2g}^*$ type. Just above the Fermi level, the orbital character changes to d$_{z^2}^*$ (Figure 25e). The nonbonding nature of surface states
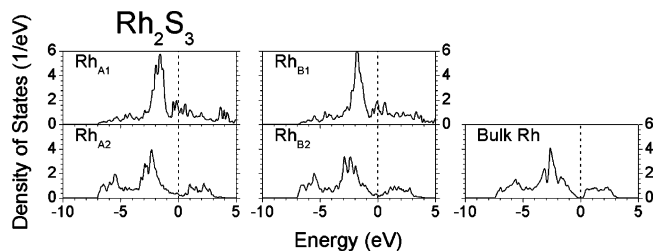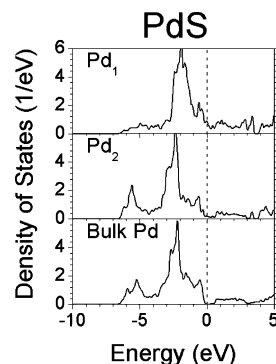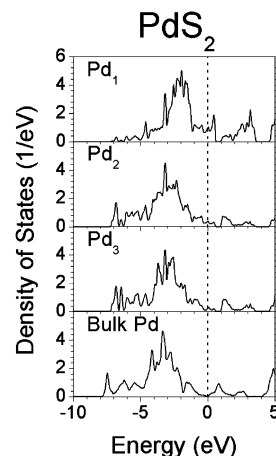
around the Fermi level is preserved as found in the previous sulfides. The intensity of the corresponding peak below the Fermi level increases in comparison to the TcS$_2$ case (Figures 20 and 21), revealing the enhanced back-donating mechanism in RuS$_2$ and that, at the same time, it is a good acceptor because of the surface orbitals on metallic sites above the Fermi level. It is worth mentioning that just below the Fermi level the exposed Ru local DOS exhibits a narrow peak coming from the t$_{2g}^*$ band and has a reinforced nonbonding nature provoked by the narrow ∼0.5 eV width. Thus, the highest HDS activity of RuS$_2$(001) is related to the robustness of the nonbonding t$_{2g}$ states.

3.3.6. Rh$_2$S$_3$(001). At surface metal atoms, the shifting of some antibonding e$_g$ states shifts the local DOS around the Fermi level to higher energies (Figure 22). The t$_{2g}$ states peak with strong Rh atom character and, ranging from approximately −1.5 to −1.1 eV, become narrower due to the lack of Rh−Rh bonds. In comparison to the case of RuS$_2$(001), the local DOS around the Fermi level is low. In addition, the intensity of the related peaks above the Fermi level decreases. Thus, the donation−
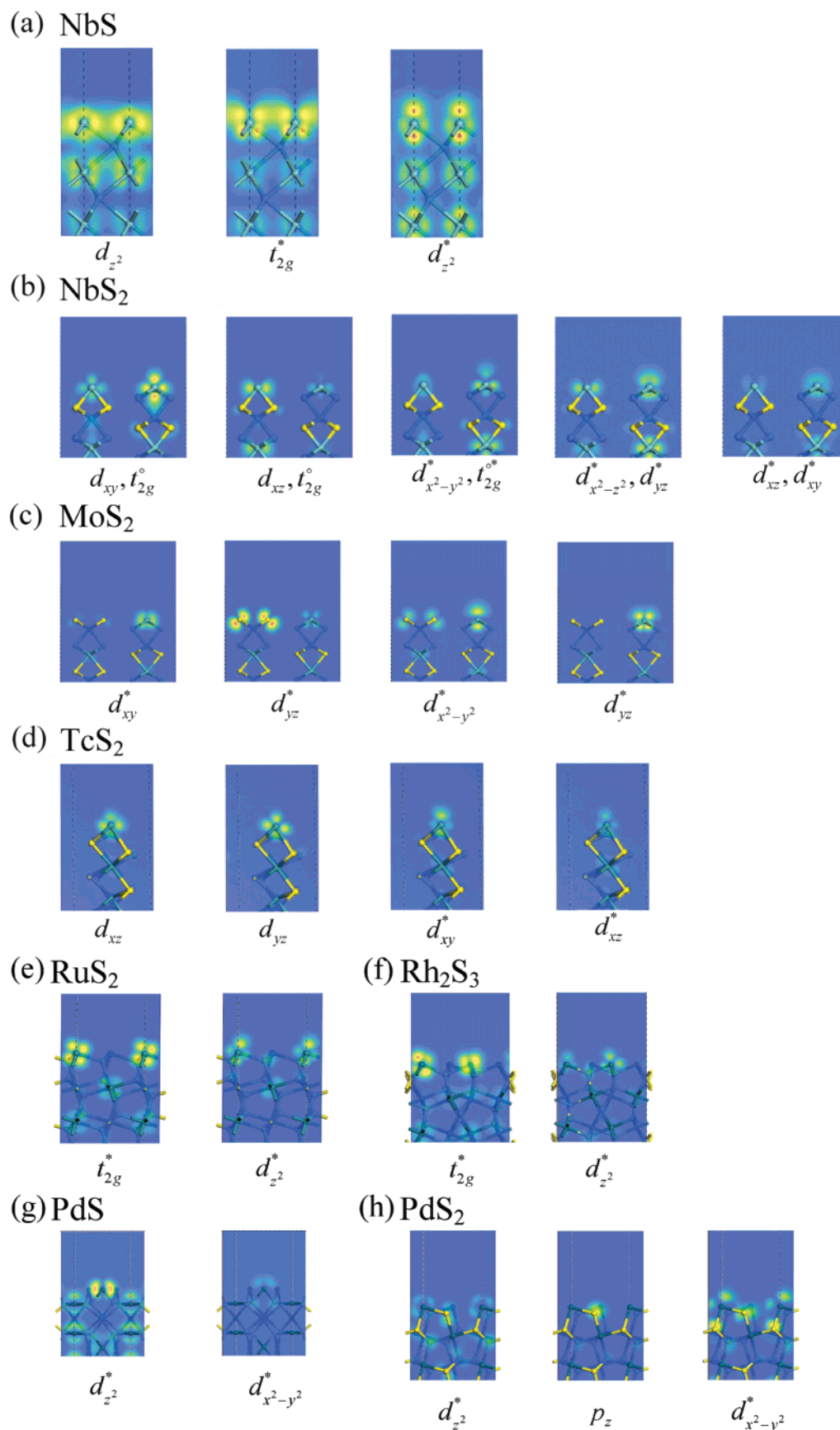
Figure 25. Electron densities for surface states near the Fermi level: (a) NbS, (b) NbS_2, (c) MoS_2, (e) RuS_2, (f) Rh_2S_3, (g) PdS, and (h) PdS_2.

back-donation mechanism is not as efficient for this sulfide as in the RuS_2 sulfide.

3.3.7. PdS(001). The local DOS at surface metallic sites does not largely change relative to the bulk case due to the low sulfur

HDS of 4d-Transition-Metal Sulfides

J. Phys. Chem. B, Vol. 110, No. 15, 2006 **7965**

coordination around Pd atoms (Figure 23). There is only a modest increase of the DOS above the Fermi level. Below and above this level the orbitals are of the $d^*_{x^2-y^2}$ type (Figure 25g). Despite their electron densities, these states are nonbonding states. This would allow a good HDS activity of this PdS surface.

3.3.8. PdS$_2$(001). As in the case of PdS(001), the local DOS related to exposed metal sites is not very different from the bulk case (Figure 24). However, there is a noticeably larger contribution below the Fermi level because of the shift of the e_g states (Figure 25h). The shift is more favorable than that in PdS(001) due to the increased concentration of sulfur atoms. The HDS activity for PdS$_2$(001) would not be better than that for PdS since the orbitals at the Fermi level are centered over sulfur atoms instead of metal ones.

4. Discussion and Conclusions

The complete set of results above presented reinforces the argument about the importance of transition metal sulfide covalent bonding in their HDS activity. This is in agreement with the arguments of Raybaud et al. for bulk MoS$_2$.[7] Nevertheless, the detailed electronic-structure analysis supports the idea that, due to the covalent interaction, predominantly d metal states exist both below and above the Fermi level in bonding and antibonding combinations, respectively. Moreover, in addition to the antibonding $(t^o_{2g}-S3p)^*$ states located at the top of the valence band, there are also bonding $t^o_{2g}-S3p$ states at the bottom of the sulfur p band; the e_g Ru levels hybridize and further split into low-energy bonding e_g-S3p and high-energy antibonding $(e_g-S3p)^*$ states. Hence, the semiconducting character of RuS$_2$ appears because the Fermi level lies at the top of almost nonbonding $(t_{2g}-S3p)^*$ states, which are separated from the bottom of the conduction antibonding $(e_g-S3p)^*$ states.

Overall, the intensities of the related valence state peaks in the DOS for the bulk configuration qualitatively show the variations of the covalent bond strength depending on the current transition metal atoms, crystal structure, and symmetry. The snapshots in Figure 7 agree in general with the order suggested in Table 5. NbS is clearly an ionic solid due to the major contributions from sulfur atoms to e_g-S3p hybrids and from niobium atoms to $t_{2g}-S3p$, $(t_{2g}-S3p)^*$, and $(e_g-S3p)^*$ hybrids. Likewise, NbS$_2$ has also an ionic character because of the main sulfur weight to $t^o_{2g}-S3p$, e_g-S3p, and $t^\pm_{2g}-S3p$ hybrids, while $(t^o_{2g}-S3p)^*$ is centered on niobium atoms.

Although MoS$_2$ valence orbital states are similar to those of NbS$_2$, we note an increased intensity of $t^o_{2g}-S3p$, e_g-S3p, and $t^\pm_{2g}-S3p$ hybrid-related peaks at metal sites, leading to a change in bonding character with an increased covalent character. TcS$_2$ has an evident covalent nature as shown by the almost equal hybrid intensities on both metal and chalcogen atoms. Although RuS$_2$ is considered as a covalent solid, Figure 7e shows that the covalent contribution arises only from the valence e_g-S3p states. Nevertheless, RuS$_2$ is more covalent than TcS$_2$ since the RuS$_2$ e_g DOS intensity is larger than that of TcS$_2$ valence orbitals. Still, Rh$_2$S$_3$ is more covalent than RuS$_2$ because the latter exhibits nonbonding states whereas in the former all of the orbitals contribute to bonding or antibonding hybrids. It is expected that PdS and PdS$_2$ are among the most covalent TMSs because of the low coordination of the sulfur atoms. An inspection of Figure 7 shows that for bulk sulfides the orbitals contributing to covalent bonding are e_g-S3p (MoS$_2$), e_g-S3p (TcS$_2$), e_g-S3p (RuS$_2$), $t_{2g}-S3p$ (Rh$_2$S$_3$), $b_{1g}-S3p$ (PdS), and $b_{1g}-S3p$ (PdS$_2$). Their respective energy intervals (Table 6) qualitatively suggest that the lower the covalence energy range

relative to Fermi level, the narrower the energy gap is. The covalent-band depth offers a possible explanation for the validity of the Sabatier principle; the cohesive energy of the above sulfides is dominated by covalent bands near to the Fermi level, and these are also the levels involved in chemical reactions. Among the semiconducting sulfides, only RuS$_2$ has nonbonding hybrids just at the Fermi level, which could be relevant to HDS activity since these bulk states are not involved in bonding with the sulfide sulfur and then they are able to interact with external hydrocarbon sulfur instead.

As it is expected, the energy gap of bulk semiconducting sulfides is populated by surface states that appear when the sulfides are cleaved. In the case of NbS and NbS$_2$ it is difficult to generate pure surface states (Figures 25a and 25b) because the bulk metallic character leads to extended states through the slab volume. In NbS, the delocalized character of the $d^*_{z^2}$ states above the Fermi level reduces the available number of states able to allocate donated electrons, e.g., from organosulfur molecules. The NbS$_2$ surface could be a better HDS catalyst than NbS because of the more localized nature of the relevant states. However, its HDS activity is limited due to the penetration of the states, both below and above the Fermi level, into the deeper slab atomic layers. Moreover, the partial DOS on Nb atoms (Figure 18) reveals that the peaks of the states participating in the donation−back-donation mechanism are not as intense as in the RuS$_2$ case (see below). The MoS$_2$ surface, although being a good electron receptor, cannot donate efficiently because of the small intensity of states just below the Fermi level (Figures 19 and 25c). Nevertheless, the large surface character of states is responsible for the higher MoS$_2$ HDS activity compared to the corresponding NbS and NbS$_2$ surfaces. Available states for the donation−back-donation mechanism and their almost pure surface nature exist in the TcS$_2$ slab, and this should increase the HDS activity relative to that of MoS$_2$. For the best experimental HDS catalyst, RuS$_2$, the slab model DOS exhibits the most intense surface states both below and above the Fermi level. The Rh$_2$S$_3$ surface has a good back-donation capability but fails in the donation step; thus, its catalytic behavior diminishes relative to RuS$_2$. The PdS slab has low-intense surface states around the Fermi level, thus with a concomitant decrease of the catalytic activity. The present study suggests that the PdS$_2$ surface was not a good HDS catalyst because it does not have Pd d states to back-donate electrons.

The orbital symmetry by itself is also important. It was suggested that the bonding between the sulfur of a thiophenic molecule and the transition metal is of the π type. The surface sulfide electron states below the Fermi level for the predicted good catalysts—MoS$_2$(d^*_{yz}), TcS$_2$(d_{yz}), and RuS$_2$(t_{2g})—all have the appropriate orbital shape at metal sites to back-donate electrons in π bonding (Figure 25). These orbitals are well distinguished from those lying above the Fermi level (Table 8). The Rh$_2$S$_3$ surface also has the required orbital symmetry, although this extends continuously from below to above the Fermi level. The NbS surface has t^*_{2g} hybrids just below the Fermi level as in the RuS$_2$ case, but these are poisoned with $d^*_{z^2}$ ones. The NbS$_2$ surface orbitals do not have the convenient position below the Fermi level but instead just very near or above it. The PdS surface does also have orbitals that favor the π molecule−catalyst bonding, but their DOS intensities are low and extend continuously over an energy interval containing the Fermi level. Notice that the PdS$_2$ surface does not have Pd d contributions below the Fermi level and hence the HDS activity must be vanishing. Finally, notice that at reactor temperature ($\sim$700 K) the catalyst electron states participating in the HDS

Oviedo-Roa et al.

activity come from an energy interval $k_BT \approx 0.05$ eV below the Fermi level. This ensures that in the RuS_2 surface electrons back-donate entirely from the very narrow DOS peak $(t_{2g}-S3p)^*$ states, which are essentially nonbonding either in bulk or in the surface.

In summary, we presented a density functional theory study within the periodic plane-wave pseudopotential approach aimed to uncover the catalyst electronic properties that may be relevant in the HDS activity of 4d-transition-metal sulfides. To describe the bulk DOS we emphasized the importance of both electrostatic and covalent splitting of transition metal d states due to the sulfur coordination. Although most of the studied bulk sulfides are clearly covalent solids, they can exhibit energy bands of ionic character. Covalent splitting opens a semiconducting gap that increases with the depth of the covalent states relative to the Fermi energy. This is in agreement with the Sabatier principle since the cohesive energy of the studied sulfides has contributions mostly from the valence covalent states, and the nearest to the Fermi level is mostly responsible for the chemical HDS activity.

The present study suggests that the best HDS catalytic activity is found when the bulk catalyst has semiconductor character and nonbonding states at metal sites are located just below the Fermi level. The semiconducting character persists in the sulfide surface due to the incomplete filling of the energy gap by surface metallic states. The nonbonding character allows orbitals to interact with sulfur atoms of incoming molecules. These orbitals must be t_{2g} hybrids since in this way they can better interact with sulfur-containing molecules in a π-type bonding. The fact that $t_{2g}-S3p$ states are located below the Fermi level indicates that they can back-donate electrons to the thiophenic-like incoming molecule lowest unoccupied molecular orbital (LUMO). Populating the molecule LUMO with catalyst electrons is essential in the HDS process since it leads to the weakening of sulfur–carbon bonds. Thus, it is necessary to have a high number of $t_{2g}-S3p$ states below the Fermi level, which ideally should concentrate in a very narrow DOS peak. This is due to the k_BT small-size energy interval able to efficiently back-donate electrons. At the same time, the sulfide must be a good electron acceptor to attract the donor sulfur-containing molecule, hence with a conduction DOS peak just above the Fermi level. Thus, the best HDS catalyst should have a local DOS minimum at the Fermi level on exposed metal atoms. Finally, we note that the conclusions reported in this paper could be extended to the 5d-transition-metal sulfides, since the plot of HDS activity versus transition metal position in the periodic table has a very similar behavior to that of 4d-transition-metal sulfides and crystal structures for chalcogenide species are analogous within the same periodic transition metal group.

References and Notes

(1) Pecoraro, T. A.; Chianelli, R. R. *J. Catal.* **1981**, *67*, 430.
(2) Chianelli, R. R. *Catal. Rev. Sci. Eng.* **1984**, *26*, 361.
(3) Vissers, J. P. R.; Groot, C. K.; van Oers, E. M.; de Beer, V. H. J.; Prins, R. *Bull. Soc. Chim. Belg.* **1984**, *93*, 813.
(4) Ledoux, M. J.; Michaux, O.; Agostini, G. *J. Catal.* **1986**, *102*, 275.
(5) Harris, S.; Chianelli, R. R. *J. Catal.* **1984**, *86*, 400.
(6) Raybaud, P.; Kresse, G.; Hafner, J.; Toulhoat, H. *J. Phys.: Condens. Matter* **1997**, *9*, 11085.
(7) Raybaud, P.; Kresse, G.; Hafner, J.; Toulhoat, H. *J. Phys.: Condens. Matter* **1997**, *9*, 11107.
(8) Raybaud, P.; Hafner, J.; Kresse, G.; Toulhoat, H. *Phys. Rev. Lett.* **1998**, *80*, 1481.
(9) Hobbs, D.; Hafner, J. *J. Phys.: Condens. Matter* **1999**, *11*, 8197.
(10) Rohrbach, A.; Hafner, J.; Kresse, G. *J. Phys.: Condens. Matter* **2003**, *15*, 979.
(11) Gómez-Balderas, R.; Oviedo-Roa, R.; Martínez-Magadán, J. M.; Amador, C.; Dixon, D. A. *Surf. Sci.* **2002**, *518*, 163.
(12) Toulhoat, H.; Raybaud, P.; Kasztelan, S.; Kresse, G.; Hafner, J. *Catal. Today* **1999**, *50*, 629.
(13) Chianelli, R. R.; Berhault, G.; Raybaud, P.; Kasztelan, S.; Hafner, J.; Toulhoat, H. *Appl. Catal., A* **2002**, *227*, 83.
(14) Aray, Y.; Rodríguez, J. *ChemPhysChem* **2001**, *10*, 599.
(15) Kasztelan, S.; Jalowiecki, L.; Wambeke, A.; Grimblot, J.; Bonnelle, J. P. *Bull. Soc. Chim. Belg.* **1987**, *96*, 1003.
(16) Wambecke, A.; Jalowiecki, L.; Kasztelan, S.; Grimblot, J.; Bonnelle, J. P. *J. Catal.* **1988**, *109*, 320.
(17) Raybaud, P.; Hafner, J.; Kresse, G.; Kasztelan, S.; Toulhoat, H., *J. Catal.* **2000**, *189*, 129.
(18) Raybaud, P.; Hafner, J.; Kresse, G.; Kasztelan, S.; Toulhoat, H., *J. Catal.* **2000**, *190*, 128.
(19) Grillo, M. E.; Sautet, P. *Surf. Sci.* **2000**, *457*, 285.
(20) Raybaud, P.; Hafner, J.; Kresse, G.; Toulhoat, H. *Surf. Sci.* **1998**, *407*, 237.
(21) Colell, H.; Bronold, M.; Fiechter, S.; Tributch, H. *Surf. Sci. Lett.* **1994**, *303*, 361.
(22) Payne, M. C.; Teter, M. P.; Allan, D. C.; Arias, T. A.; Joannopolous, J. D. *Rev. Mod. Phys.* **1992**, *64*, 1045.
(23) Hammer, B.; Hansen, L. B.; Nørskok, J. K. *Phys. Rev. B* **1999**, *59*, 7413.
(24) Vanderbilt, D. *Phys. Rev. B* **1990**, *41*, 7892.
(25) Kresse, G.; Furthmüller, J. *Phys. Rev. B* **1996**, *54*, 11169.
(26) Delley, B. *J. Chem. Phys.* **1990**, *92*, 508.
(27) Segall, M. D.; Shah, R.; Pickard, C. J.; Payne, M. C. *Phys. Rev. B* **1996**, *54*, 16317.
(28) Segall, M. D.; Pickard, C. J.; Shah, R.; Payne, M. C. *Mol. Phys.* **1996**, *89*, 571.
(29) Davidson, E. R.; Chakravorty, S. *Theor. Chim. Acta* **1992**, *83*, 319.
(30) Sánchez-Portal, D.; Artacho, E.; Soler, J. M. *Solid State Commun.* **1995**, *95*, 685.
(31) Sánchez-Portal, D.; Artacho, E.; Soler, J. M. *J. Phys.: Condens. Matter* **1996**, *8*, 3859.
(32) Huheey, J. E.; Keiter, E. A.; Keiter, R. L. *Inorganic Chemistry: Principles of Structure and Reactivity*; Benjamin Cummings: Reading, MA, 1997.
(33) Ballhausen, C. J. *Introduction to Ligand Field Theory*; McGraw-Hill: New York, 1962.
(34) Topsoe, H.; Clausen, B. S. *Catal. Rev. Sci. Eng.* **1984**, *26*, 395.
(35) Bouwens, S. M. A. M.; van Veen, J. A. R.; Koningsberger, D. C.; de Beer, V. H. J.; Prins, R. *J. Phys. Chem.* **1991**, *95*, 123.